JGR Atmospheres

RESEARCH ARTICLE
10.1029/2022JD038207

Trend and Multi-Frequency Analysis Through Empirical Mode Decomposition: An Application to a 20-Year Record of Atmospheric Carbonyl Sulfide Measurements

C. Serio[1], S. A. Montzka[2], G. Masiello[1], and V. Carbone[3]

[1]Scuola di Ingegneria, Università degli Studi della Basilicata, Potenza, Italy, [2]NOAA Global Monitoring Laboratory, Boulder, CO, USA, [3]Dipartimento di Fisica, Università della Calabria, Rende, Italy

Key Points:

- Atmospheric carbonyl sulfide has decreased at NOAA network stations in recent years
- Time Series Analysis and trend identification
- Empirical Mode Decomposition identified many characteristic frequencies of variability, some compatible with Quasi Biennal Oscillation

Supporting Information:

Supporting Information may be found in the online version of this article.

Correspondence to:

C. Serio,
carmine.serio@unibas.it

Citation:

Serio, C., Montzka, S. A., Masiello, G., & Carbone, V. (2023). Trend and multi-frequency analysis through Empirical Mode Decomposition: An application to a 20-year record of atmospheric carbonyl sulfide measurements. *Journal of Geophysical Research: Atmospheres*, *128*, e2022JD038207. https://doi.org/10.1029/2022JD038207

Received 22 NOV 2022
Accepted 8 JAN 2023

Author Contributions:

Conceptualization: C. Serio
Data curation: S. A. Montzka
Formal analysis: S. A. Montzka, V. Carbone
Funding acquisition: C. Serio
Investigation: G. Masiello
Methodology: C. Serio, V. Carbone
Resources: G. Masiello
Software: C. Serio, G. Masiello, V. Carbone
Supervision: S. A. Montzka
Validation: C. Serio
Visualization: G. Masiello
Writing – original draft: C. Serio

Abstract The Empirical Mode Decomposition (EMD) is a fully non-parametric analysis of frequency modes and trends in a given series that is based on the data alone. We have devised an improved strategy based on a series of *best practices* to use EMD successfully in the analysis of the monthly time series of carbonyl sulfide (OCS) atmospheric mole fractions measured at NOAA network stations (2000–2020). Long-term trends and intra- and inter-annual variability has been assessed. After a phase of generally increasing mole fractions up to 2015, with a temporary decline around 2009, we found that the OCS atmospheric mole fraction subsequently decreased at all stations, reflecting a recent imbalance in its total sources and losses. Our analysis has revealed a characteristic time scale for variation of 8–10 years. The variance associated with this long-term behavior ranges from ∼15% to 40% of the total strength of the signal, depending on location. Apart from this complex long-term behavior, the OCS time series show a strong annual cycle, which primarily results from the well-known OCS uptake by vegetation. In addition, we have also found one more frequency of minor variance intensity in the measured mole fraction time-history, which corresponds to periods in the range of 2–3 years. This inter-annual variability of OCS may be linked to the Quasi-Biennial Oscillation.

Plain Language Summary The Empirical Mode Decomposition has arisen as a new paradigm for the processing and analysis of time series. The tool has been applied to multi-year mole fraction measurements of an atmospheric gas, carbonyl sulfide (OCS), which has important implications for understanding and analyzing the carbon cycle. OCS is the most abundant sulfur-containing trace gas in the atmosphere and has recently emerged as a putative proxy for the terrestrial photosynthetic uptake of CO_2 because OCS and CO_2 have the same diffusion pathway into leaves. The study has analyzed OCS at 14 cooperative stations, which are distributed all around the world. We have found a characteristic time scale for 8–10 years variation. Apart from this complex long-term behavior, the OCS time series show a robust yearly cycle, primarily from OCS uptake by vegetation. Finally, we have also found one more frequency, which corresponds to periods in the range of 2–3 years. This inter-annual variability of OCS may be linked to the Quasi-Biennial Oscillation, which is an almost periodic oscillation of the winds of the equatorial stratosphere.

1. Introduction

The paper addresses the analysis of 20-year records of atmospheric carbonyl sulfide (OCS) measurements from the National Oceanic and Atmospheric Administration (NOAA) global flask network with Empirical Mode Decomposition (EMD, Huang et al., 1998). The EMD separates a given time series in its primary cycles plus a trend. The method is non-parametric, and there is no need to specify a trend model as generally done with other approaches. EMD has been successfully applied in many fields (e.g., Capparelli et al., 2013; Stallone et al., 2020). EMD is more suitable than traditional methods for analyzing nonlinear and nonstationary signals, whose statistical properties (e.g., mean and standard deviation) change over time. However, the straightforward applications of the technique could lead to misuse if its known limitations and basic assumptions are not carefully considered. EMD still has some open issues about its formal characterization when operating on a broadband signal, such as white noise (e.g., Wu & Huang, 2010). Taking advantage of the recent work by Stallone et al. (2020) who provided best practices to maximize the quality and meaningfulness of EMD, we have devised a tool and applied it to the OCS time series for the analysis of trends, seasonal cycle, and inter-annual variability. The tool is general and can be used for the analysis of other atmospheric parameters.

Writing – review & editing: S. A. Montzka

The importance of OCS in the study of terrestrial vegetative ecosystems has clearly emerged in recent studies (Campbell et al., 2008; Maseyk et al., 2014; Montzka et al., 2007). OCS is the most abundant sulfur-containing trace gas in the atmosphere and accounts for a significant part of sulfur in the stratospheric aerosol (Brühl et al., 2012). Essential sources of OCS are natural; oceans and soils play a dominant role with a more negligible contribution from volcanic activity (Whelan et al., 2018). The ocean is the main natural source of OCS, and it has been estimated that the oxidation of dimethyl sulfide (DMS) emitted from the sea surface accounts for 8%–20% of the global OCS source (Jernigan et al., 2022). In addition to DMS, atmospheric CS_2 oxidation represents an important anthropogenic source of OCS (c.a. 30% Chin & Davis, 1993). Otherwise, anthropogenic sources have been recognized as secondary contributors: biomass burning and industrial activities (e.g., Whelan et al., 2018). The main sink of OCS has been identified as vegetation uptake, whose magnitude is also influenced by seasonal trends in terrestrial vegetative photosynthesis. Conversely, in the stratosphere, the photochemical loss is the prominent removal process, but at a substantially slower rate than vegetative uptake (Kettle, 2002; Whelan et al., 2018).

Moreover, OCS has emerged as a putative proxy for the terrestrial photosynthetic uptake of CO_2 because OCS and CO_2 have the same diffusion pathway into leaves (e.g., Notni et al., 2007; Protoschill-Krebs & Kesselmeier, 1992; Schenk et al., 2004), and OCS hydration reaction in this process is irreversible. In addition (Montzka et al., 2007) and more recent works (Berry et al., 2013; Campbell et al., 2015) have shown that OCS holds great promise for studies of carbon cycle processes because it is an atmospheric tracer of photosynthetic Gross Primary Production (GPP). According to Berry et al. (2013), Campbell et al. (2015), and Montzka et al. (2007), the uptake of OCS from the atmosphere is dominated by carbonic anhydrase (CA), an enzyme abundant in leaves that also catalyzes CO_2 hydration during photosynthesis. However, as a continuation of previous studies, it has been shown by Ogée et al. (2016) that soils can also effectively exchange OCS with the atmosphere, which can complicate the retrieval of GPP from atmospheric budgets for some regions and scales. Some agricultural fields can take up large amounts of OCS from the atmosphere as soil microorganisms contain CA. OCS emissions from soils have been reported in agricultural fields or anoxic soils (Ogée et al., 2016).

Apart from seasonal variations, the OCS atmospheric mole fraction had remained relatively stable, for example, within 7% (Montzka et al., 2007) for the period 2000–2005, when OCS routinely began measured at most of the 18 NOAA stations and aircraft profiling sites. Ice core and firm air measurements (e.g., Aydin et al., 2020) and references therein, have been used to reconstruct atmospheric carbonyl sulfide's preindustrial and industrial history. The more recent atmospheric OCS abundance surveys use a panoply of complementary ground-based, airborne, and satellite observations (e.g., Camy-Peyret et al., 2017; Krysztofiak et al., 2015; Lejeune et al., 2017; Montzka et al., 2007).

Almost all analyses of historical and contemporary data sets (Campbell et al., 2017) have been interpreted with models that simulate changes in OCS concentration according to changes in the global budget of natural and anthropogenic sources (from oceans and soils, from industry and biomass burning, respectively), and biogenic sinks (from plant photosynthesis and soils) as reviewed by Whelan et al. (2018). Although anthropogenic emissions have exerted a dominant influence in driving atmospheric abundance changes since the 19th century (Aydin et al., 2020; Montzka et al., 2004), various studies (e.g., Aydin et al., 2020; Campbell et al., 2015) found that long-term changes in the atmospheric OCS were also influenced by considerable growth in plant photosynthesis during the twentieth century. However, these analyses did not encompass the most recent trends in atmospheric OCS, for example, since 2014–2015, which is done in the current study and by other recent studies (Hannigan et al., 2022). Hannigan et al. (2022) analyzed OCS observations, recorded with solar absorption FTIR remote sensing, from 22 globally distributed NDAAC (Network for the Detection of Atmospheric Composition) stations between 1986 and 2020. In this respect, our study complements the analyses by Kremser et al. (2015), Lejeune et al. (2017), and Hannigan et al. (2022) that are based on solar absorption FTIR remote sensing, because ours stems from an analysis of in situ near-surface flask measurements and therefore allows us to corroborate findings regarding the long-term tropospheric variability of OCS with an independent data set.

Using EMD, this study analyzes OCS measurements from the NOAA's global flask network, whose observing stations are spread around the globe but are more numerous in the North Hemisphere (NH), where anthropogenic sources are localized. A qualitative inspection of these data shows that atmospheric OCS mole fractions have entered a decline phase at all stations in recent years (through 2020). The quantitative EMD analysis will show that a long-term behavior with a characteristic variability time scale of ~8–10 years characterizes OCS time series from all sites analyzed in this study. In addition, the analysis will also show cyclic behaviors with

Table 1
Locations Where OCS Mole Fractions Are Regularly Measured From Flask Samples Have Been Analyzed in This Study

Station	Code	Lat (°N)	Lon (°W)	Elev (m)	Time interval endpoints	$\overline{X}$ (ppt)	σ_X (ppt)	$\overline{\sigma}_d$ (ppt)	$\overline{\sigma}_{dm}$ (ppt)	% missing data
Alert, Nunavut, Canada	ALT	82.4508	62.5072	185	May 2000–October 2020	453.8	39.64	2.21	13.0	12.60
Point Barrow, USA	BRW	71.3230	156.6114	11	March 2000–December 2020	456.5	40.87	1.68	12.2	2.40
Cape Grim, Tasmania	CGO	−40.683	144.6900	94	February 2000–December 2020	490.0	14.76	1.95	4.4	3.60
Harvard Forest, USA	HFM	42.5378	72.1714	340	March 2000–December 2020	441.2	49.53	1.72	16.4	2.40
Cape Kumukahi, USA	KUM	19.7371	155.0116	0.30	March 2000–December 2020	504.8	22.48	1.69	11.2	0.80
Park Falls, USA	LEF	45.9451	90.2732	472	May 2000–December 2020	445.4	44.77	1.60	18.3	2.01
Mace Head, Ireland	MHD	53.3260	9.899	5.00	May 2001–December 2020	479.6	33.35	1.63	9.8	7.60
Mauna Loa, USA	MLO	19.5362	155.5763	3,397	March 2000–December 2020	503.8	17.90	1.67	8.8	0.40
Niwot Ridge, USA	NWR	40.0531	105.586	3,523	March 2000–December 2020	498.0	19.91	1.95	10.9	3.20
Palmer Station, Antarctica	PSA	−64.774	64.0527	10	May 2000–December 2020	502.8	20.03	1.91	4.4	14.50
Tutuila, American Samoa	SMO	−14.247	170.564	42	March 2000–December 2020	501.9	12.85	2.13	8.7	2.80
South Pole, Antarctica	SPO	−89.98	24.8	2,810	May 2000–December 2020	490.7	14.69	1.50	3.6	11.29
Summit, Greenland	SUM	72.5962	38.422	3,209	June 2004–December 2020	476.7	34.19	1.34	9.6	5.03
Trinidad Head, USA	THD	41.0541	124.151	107	April 2002–December 2020	467.4	41.40	1.45	32.5	0.44

Note. The table also gives the values of $\overline{X}$, σ_X, $\overline{\sigma}_d$, and $\overline{\sigma}_{dm}$ and the percentage of missing data, as monthly means, for each time series (see text for definitions of these terms). These gaps represent months without any measurements, and they can result from a lack of availability of flasks at a site or larger-than-acceptable differences in simultaneously filled flasks.

annual and inter-annual scales of variability over-imposed on this trend, which seem to change with time. EMD is better suited than the usual Fourier analysis to study processes whose characteristic time-space scales of variability change with time. To exemplify this is the case of quasi-periodic signals, which encompass critical atmospheric processes such as El-Nino and the Quasi-Biennial Oscillation (QBO) (e.g., see Baldwin et al., 2001; Sun et al., 2018).

The paper is organized as follows. First, Section 2 describes data and methods. Then, Section 3 is devoted to presenting and discussing results. Finally, conclusions are presented in Section 4.

2. Data and Methods

2.1. Data

For many years, OCS measurements from flasks have been obtained at approximately weekly intervals at 14 NOAA and cooperative stations (Montzka et al., 2007). The sampling process involves simultaneously pressurizing air into a pair of stainless steel or glass flasks that are subsequently shipped to the Boulder laboratory for analysis. Standards are prepared in-house at the NOAA laboratory. For more details, see Montzka et al. (2007). Data used in this analysis are posted and regularly updated at the NOAA website (e.g., see Global Monitoring Laboratory, 2022). The precision of each sampling event is derived by computing the standard deviation σ_d of the mole fraction measured in each of the two simultaneously filled flasks (flask pair difference). An analysis of these standard deviations by sites shows precision in the range of 1.5–2 ppt (1σ). The average $\overline{\sigma}_d$ of σ_d over the whole ensemble of flask pairs collected during 2000–2020 is given in Table 1 for each station. However, we stress that the instrument error is only one piece of the expected variability of the data. An important role is also played by atmospheric variability. The assessment of this component has been performed by computing the standard deviation σ_{dm} of the flask pairs within each month. We note that while σ_d is computed on the single pair, σ_{dm} considers all of the sampling events in a month (typically a flask pair per week for a total of 4 per month). The average $\overline{\sigma}_{dm}$ of σ_{dm} over the whole ensemble of samples is given in Table 1 for each station. A detailed account of the computation of both σ_d and σ_{dm} can be found in the supplemental materials.

For the present analysis, we consider monthly mean mole fractions measured for OCS at these stations, and the data span different periods according to the station. For example, the longest OCS time series in the NOAA data

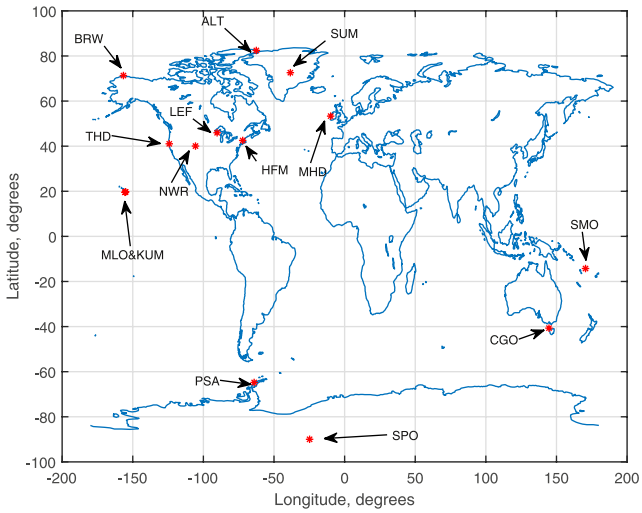

Figure 1. Location of the 14 NOAA stations considered in this work.

extends from March 2000 to December 2020. We also stress that instrument noise and atmospheric variability are both parts of any estimate of a monthly mean. Table 1 shows that the dominant player affecting the uncertainty on a monthly average is atmospheric variability.

The monthly mean time series at each site can have occasional missing data (see also the last column in Table 1); when needed, gaps in the OCS measurement records have been filled by cubic spline interpolation. An example is shown in Figure 2. Because flasks are not sampled concurrently at all sites each week, this analysis is performed on monthly means that are derived from the simple average of all flask pair sampling during each month. We also note that the uneven sample frequency, within each month, at the same station adds a sampling noise, which the EMD methodology is capable of filtering out, as will be shown further in the paper.

The monthly mean mole fraction time series will be referred to as $X(t)$, with t the time in months. Because the series X is sampled at discrete time $t = j\Delta t, j = 1, \ldots, N$, with N representing the total number of discrete measurements, we have that the whole time span of the series is $N\Delta t$. In our case, $\Delta t = 1$ month. Furthermore, to simplify notation, hereafter, we will write j for $j\Delta t$ and N for $N\Delta t$. With this in mind, the overall average of the series and standard deviation will be denoted with $\overline{X}$ and σ_X, respectively. They are computed as usual,

$$\overline{X} = \frac{1}{N}\sum_{j=1}^{N} X(j);\ \sigma_X^2 = \frac{1}{N-1}\sum_{i=1}^{N}\left(X(j) - \overline{X}\right)^2 \quad (1)$$

Table 1 shows the values of $\overline{X}$, σ_X, $\overline{\sigma}_d$ and $\overline{\sigma}_{dm}$, and summarizes the basic information about the 14 stations and the existing NOAA data records, whereas Figure 1 shows the position of the flask collection stations around the globe.

2.2. Methods

The long-term behaviors or trends in data are identified through the EMD technique, developed to process nonlinear and nonstationary data (Huang et al., 1998). EMD decomposes a time series into a finite number of intrinsic

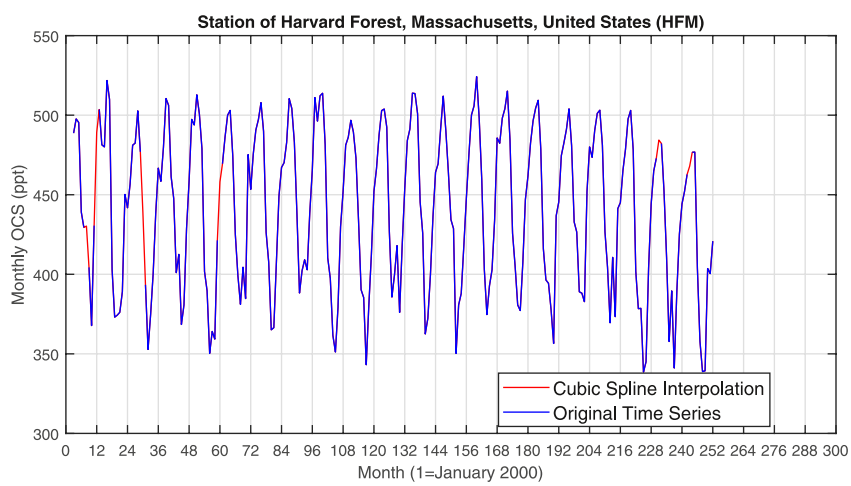

Figure 2. Example of a monthly OCS time series showing the gap-filling with cubic spline interpolation. The case shown in the figure refers to the HFM station.

mode functions (IMFs) and a residual by using an adaptive basis derived from the time series through a so-called "sifting" process, namely,

$$X(t) = \sum_{j=1}^{m} c_j(t) + r(t) \tag{2}$$

where t is the time, m the number of modes, and $X(t)$ denotes a generic time series; c_j is j-th IMF, and finally, r is the residual, which can be either the *mean* trend or a constant. Hereafter, the characteristic frequency of the mode, c_j will be denoted with f_j. Because the mode can have a frequency depending on time, f_j has to be intended as the average or peak frequency as displayed by a usual variance density spectrum analysis.

In conventional trend analysis, it is often assumed, for example, that the trend is linear, and therefore, it can be extracted with formal regression analysis (e.g., Gardiner et al., 2008; Lejeune et al., 2017). Furthermore, in non-parametric methods, the trend is analyzed through digital filtering techniques, for example, the Fourier transform and low-pass filters, to smooth the selected data and separate the low-frequency components from the seasonal cycle (e.g., Thoning et al., 1989).

In the present analysis, the trend is defined by considering all the components of the signal which show frequency modes lower than a given threshold frequency f_{th}; in this study, the default value is $f_{th} = 3/N$, that is, the frequency corresponding to a period equal to $N/3$. Because in our analysis, the OCS time series is 17–20 years long, $N/3$ yields approximately 5–7 years. The threshold has been selected by trial and error and has been checked to provide a consistent analysis for the various stations. Also, OCS has a tropospheric lifetime of ∼1.5–3 years (e.g., Montzka et al., 2007), therefore frequencies lower than f_{th} characterizes long-term trends with timescales longer than the atmospheric lifetime of OCS.

With this in mind, the trend, τ is defined according to,

$$\tau(t) = \sum_{j=l}^{m} c_j(t) + r(t) \tag{3}$$

with $f_m < \cdots . < f_l \leq f_{th}$. Again, this definition is consistent with the idea that the trend has to capture the low-frequency variability of the signal.

As already said, the characteristic frequency of a given mode, $c_j(t)$ can be identified with the usual computation of the classical Fourier variance spectrum analysis or Power Density Function (PDF). The frequency components within each IMF can be analyzed through the Huang-Hilbert transform (Huang et al., 1998). The Huang-Hilbert Transform (*hht*) is appropriate for nonstationary, nonlinear processes where the frequency modulation of the signal can change with time. The usual Fourier analysis is inadequate for these processes because it requires a representation of the signal with infinite waves of constant amplitudes and frequencies, and in real atmospheric data, these terms may not be constant. However, for atmospheric signals of OCS, which are strongly driven by the seasonal cycle, if we are interested in determining the dominant frequency of each mode, we can resort to the classical Power Density Function (PDF) analysis. For the sake of brevity and to focus more on the geophysical interpretation of results, the use of *hht* is exemplified in the supplemental materials (e.g., see Figures S32 and S33 in Supporting Information S1).

This work uses the EMD algorithm included in Matlab distribution 2020b, which implements all prescriptions and stopping criteria, as suggested by Wang et al. (2010), to avoid the decomposition to run endlessly toward the limit with infinite iterations of sifting (e.g., Wu & Huang, 2010). However, using the algorithm without careful consideration is not recommended. Even adding this stopping criteria, there is no way to prevent the code from decomposing part of the trend in the lower frequency modes. Therefore there are at least three aspects that need to be carefully addressed when using the Matlab software package: (a) how to fix the number of modes, m; (b) how to prevent mode splitting and mode mixing; (c) how to handle problems with the boundaries or end effects because of the finiteness of the series.

For issue (a), we limit the number of modes to $m = 4$, which is based on physical insights. We know that the observations are affected by sampling, instrumental, and atmospheric noise; therefore, the first mode will fit the high oscillatory component of the noise in monthly means. The second IMF or mode is expected to fit the annual cycle. The third is devoted to representing any inter-annual variability in the data series. Finally, the fourth and

last mode is to model possible lower frequency oscillations and long-term trend structures. For this reason, by default, we have the threshold criterion $f_{th} = 3/N$ in defining the trend: everything with frequency lower than $f_{th} = 3/N$ is moved to the trend. The threshold f_{th} can be changed if we are interested in looking at EMD reconstruction of the signal, which includes specific frequencies.

For issue (b), we use the Ensemble Empirical Mode Decomposition (EEMD, e.g., Wu & Huang, 2009) strategy of adding noise to the observations. For a given sample of observations, $X(j), j = 1, \ldots, N$ we build up the noise sample $\tilde{X}(j) = X(j) + w(j)$, with w a Gaussian noise term with zero mean and standard deviation, σ_w. $\tilde{X}(j)$ is EMD decomposed, and the operation is repeated *nsamples* time. Finally, the four IMF and the residual are taken by considering the average over the corresponding *nsamples*. However, before performing EMD on $\tilde{X}(j)$, we first extend the signal to account for possible boundary effects.

To this end,—issue (c), we use the strategy proposed by Stallone et al. (2020). The series $\tilde{X}(j)$ is symmetrically extended outside the boundaries, producing, on both sides, an extended signal $\tilde{X}_{ext}(j)$ which is, on each side, N times longer than the original one. Then, $\tilde{X}_{ext}(j)$ is multiplied by a function $\chi(j)$, which is one for the original signal $\tilde{X}(j)$ and tends smoothly to zero as we approach the two left and right ends of the extended signal. In this way, the signal $\tilde{X}_{ext}(j)$ is periodic at the boundaries.

For completeness, the last word has to be said for σ_w. According to Wu and Huang (2009), $w(j)$ needs to be added to the original signal to avoid the phenomenon of mode-splitting. The only important prescription is that the noise has to be white and stationary: zero mean and constant standard deviation. The value of σ_w has to be set by trial and error. By default, we use the value suggested by Wu and Huang (2009), that is, $\sigma_w = p \times \sigma_X$ with $p = 0.1$ (see Table 1 for the values of σ_X by site). The fact that σ_w is prescribed to be a fraction of σ_X just responds to the need to add a random component with a strength equal to a fraction of the total variability of the data. We also note that it is unlike that the same value of p, is good for all series. The fraction $p = 0.1$ is just to get started. A suitable p can only be found by running EMD with diverse p until the problem of mode-mixing is solved. This aspect is illustrated at a better length in the supplemental materials (e.g., see Figures S1–S3 and Table S1 in Supporting Information S1).

For the reader's benefit, we summarize the algorithm we devised to apply EMD to the OCS time series.

1. Set f_{th} (default value, $3/N$) and σ_w (default value, $\sigma_w = 0.1 \times \sigma_X$)
2. Set the maximum number of modes (default, $m = 4$)
3. Set the number of random samples (default, $nsamples = 1000$)
4. Generate the noisy series $\tilde{X}(j), j = 1, \ldots, N$
5. Generate the extended series $\tilde{X}_{ext}(j), j = 1, \ldots, 3N$
6. EMD the series $\tilde{X}_{ext}(j)$
7. Store the IMFs and the residual over the original range of the signal, $j = N + 1, \ldots, 2N$
8. Repeat steps 4 to 7 *nsamples* times
9. Compute the final IMFs and residual by considering the average over the *nsamples* of the corresponding functions calculated in step 7.
10. Compute the power density function (PDF) of the four IMF (we use the tool *pcov* in the Matlab distribution 2020b).
11. Compute the frequency peak of each IMF and related uncertainty
12. Compute the trend according to Equation 3.

It should be stressed that the above procedure has been finalized, and the sensitivity of the procedure to the various parameters checked by trial and error, simulations, and applications to the time series at hand.

3. Results and Discussion: OCS Measurements at Sites in the NOAA Network for the Year Range 2000–2020

3.1. Exemplifying EMD Through the Application to the MLO Station

To explain how the EMD decomposition is applied and used in this study, we show its application to the MLO series (monthly averages from March 2000 to December 2020 ($N = 250$ months)). The Mauna Loa site has the

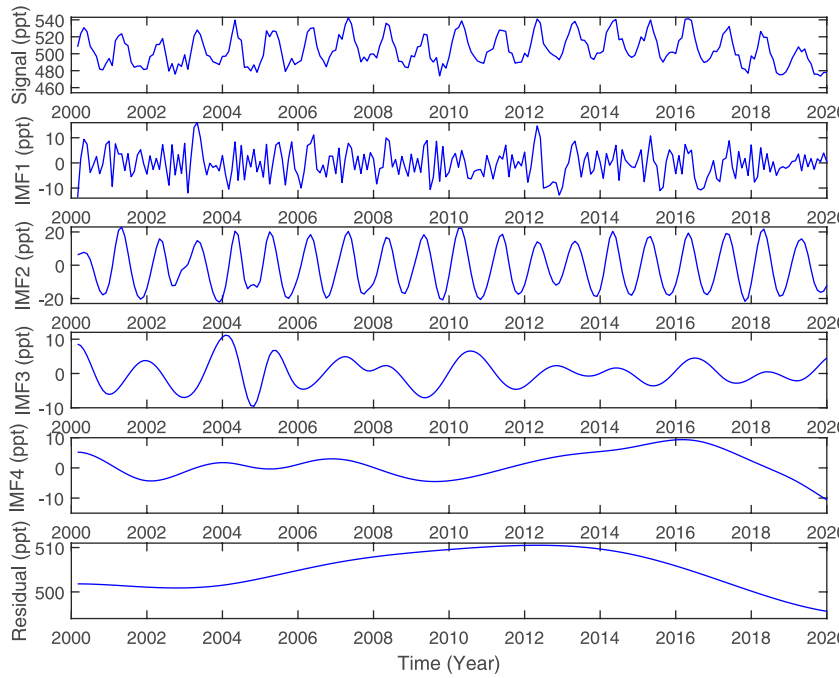

Figure 3. Exemplifying the EMD analysis applied to MLO monthly mean mole fractions measured for OCS (in ppt). Top to bottom, signal, IMFs and residual.

longest OCS record, among the 14 NOAA stations considered here, with almost no data missing. The MLO station is an important research facility that has continuously monitored and collected data related to atmospheric change since the 1950s. The choice of a single station makes it easier to show how EMD works. However, the complete EMD analysis is available in the supplemental materials for all stations (e.g., see Figures S4–S31 in Supporting Information S1).

The decomposition consists of four modes and a residual and is shown in Figure 3, and it is possible to see that the higher mode numbers are associated with lower frequency variability.

As expected, the first IMF extracts the high oscillatory component of the noise in monthly means, which includes measurement error but is comprised mostly of real atmospheric variability within each month. In effect, the maximum amplitude of IMF1 is consistent with the atmospheric variability derived directly from the measurements, or $\overline{\sigma}_{dm}$ (see Table 1). For MLO we have a value of 8.8 ppt for $\overline{\sigma}_{dm}$. The second component is an almost perfect harmonic of the constant period, although the amplitude can change with time. To better understand the relevant frequencies in the third and fourth modes, the PDFs of the four IMFs in Figure 3 are shown in Figure 4.

From Figure 4, we see that *the first IMF* has a flat spectrum, as expected for white noise, and its spectral density is two orders of magnitude lower than the sharp power of the annual cycle (there is a ratio of 100:1 in the y-axis scale of IMF2 vs. IMF1). Compared with Figure 3, it is possible to see that the EMD methodology can filter out the random component in the data arising from measurement imprecision and atmospheric variability.

The second IMF (shortened to IMF2) extracted from the MLO record yields a frequency peak almost exactly at $1/12 \cong 0.0833$ in units of 1/month. IMF2 has the most prominent spectral density; in fact, from Figure 3, we see that the mode is close to a pure harmonic with a period equal to 12 months. This aspect will be better analyzed and discussed in Section 3.2.

The third IMF (shortened to IMF3) is close to 2 years, although its uncertainty is as large as ∼6 months, and its spectral density is 1–2 orders of magnitude lower than that of the annual cycle. However, although of less intensity, the IMF3 power maximizes at a value that is in good agreement with the QBO (Quasi-Biennial Oscillation) mean cycle, which has a periodicity of 28–29 months, or ∼0.4 per year, for example, see Ray et al. (2020). The third mode and its possible relationship with QBO will be further addressed in Section 3.3.

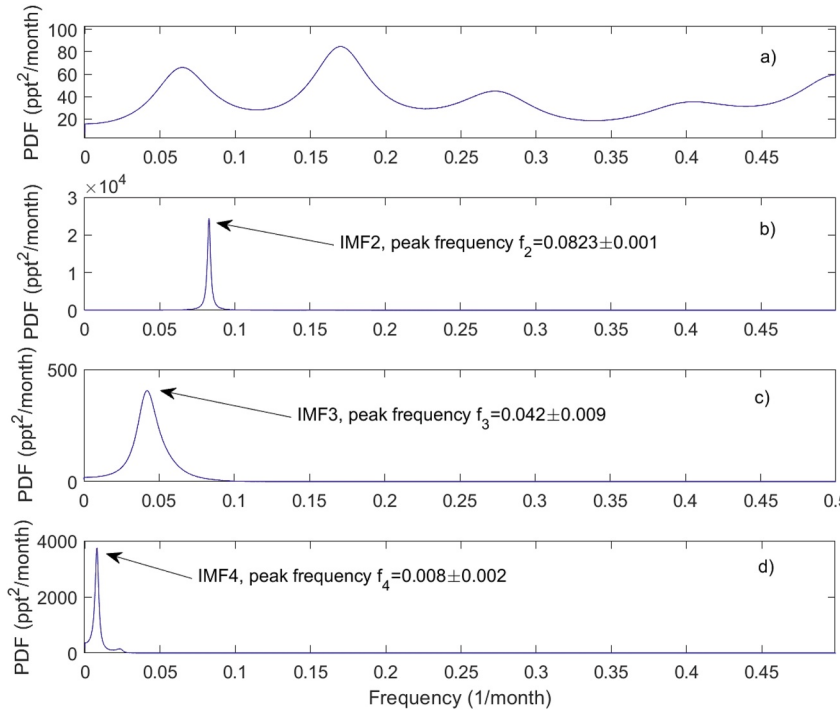

Figure 4. MLO station. Power density functions of the four IMF corresponding to the EMD decomposition of the MLO monthly time series shown on a range of vertical scales; (a) IMF1; (b) IMF2; (c) IMF3; (d) IMF4. The figure also shows the peak frequency of IMF2-4. The frequency uncertainty shown in the figure is the half-width at half-maximum of the corresponding spectral line.

The fourth mode (shortened to IMF4) is more peaked than the third. It has a larger density but corresponds to a period close to 10 years. Therefore, this mode is moved to the trend or long-term behavior shown in Figure 5. The role of the fourth mode and trend will be further discussed in Section 3.4. Here we expand and discuss the advantage of the EMD trend and its definition. According to Equation 3, the EMD trend, τ is prescribed to show time scales larger than those corresponding to the threshold frequency, $f_{th} = 3/N$, which for the MLO station corresponds to ~7 years. From Figure 5 we see that on time scales larger than 7 years, the decline of the OCS in recent years is clearly evident. Again in Figure 5, the EMD trend is compared with the other two smoothing,

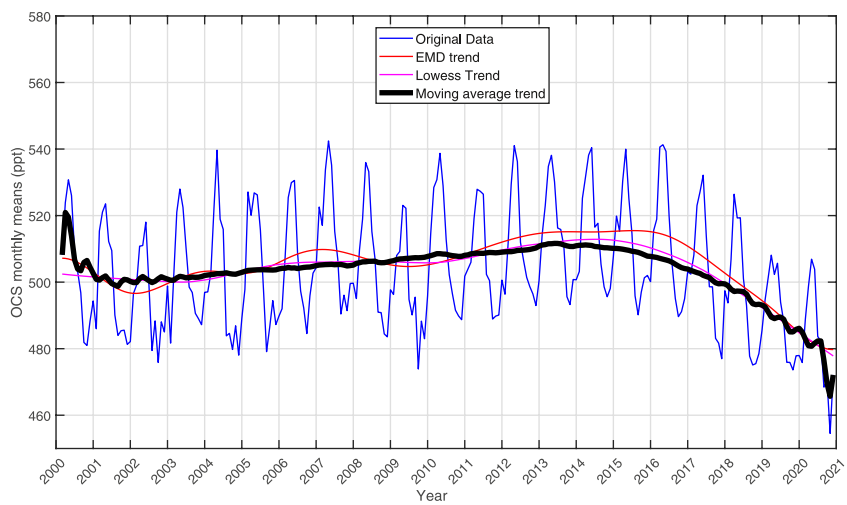

Figure 5. OCS monthly averages (2000–2020) for the MLO station and trend analysis according to EMD, *lowess* and moving average filters (e.g., see Equation 3 and the text in the paper).

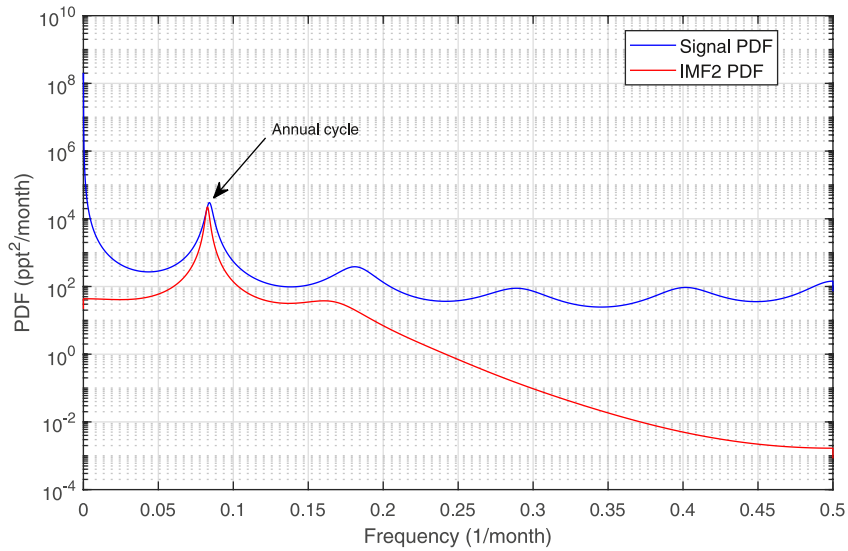

Figure 6. The power Density Function of the whole signal derived from a Fourier analysis of the MLO OCS monthly mean mole fraction time series over the past 20 years ("Signal PDF"), and the second IMF extracted through the EMD analysis.

non-parametric and nonlinear, algorithms. These are the *lowess,* τ_l (an acronym of locally weighted scatter plot smoothing, e.g., Cleveland & Devlin, 1988) and the moving average, τ_{ma}. They are both prescribed with a span of $N/3$ to properly compare with the time scales designed for the EMD trend. The *lowess* smoothing is based on a local least squares fitting and generalizes the smoothing average method, which is also shown in Figure 5. It is seen that the moving average filter shows a high-frequency ringing close to the boundaries of the signal, where it tends to collapse on the data points. In contrast, the *lowess,* τ_l is much more consistent at the boundaries, although it provides a smoother version than the EMD, τ. Nevertheless, the comparison exemplifies how EMD yields a methodology to determine and control the characteristic scales we want to include in the reconstruction of the signal.

Before closing this section, to further exemplify the advantage of EMD, we also note that a conventional Fourier analysis of the signal does not detect all of the modes identified for OCS by the EMD decomposition. Figure 6 shows the PDF of the MLO time series, whose EMD decomposition has been exemplified through Figures 3 and 4. It is seen that the Fourier analysis is capable of extracting the annual cycle. In contrast, the remaining modes, which EMD identifies in Figure 3, are lost in a broad low-pass spectrum with a zero-frequency peak. Figure 6 also shows, for comparison, the PDF of the second IMF, which extracts the annual cycle from the original signal. It can be seen that the PDF of the second IMF exactly matches the peak of the annual cycle in the PDF signal, which allows us to stress the property of EMD to extract the relevant modes from the signal. An analysis based solely on the PDF of the signal would conclude the presence of a single dominant mode and a low-pass component with a peak at zero frequency, which parallels the EMD residue and IMF4. In contrast, EMD can correctly identify the annual cycle but can also reveal a cyclic mode in the lower frequency range with a characteristic time of ∼10 years (IMF4).

3.2. The EMD Analysis of the Annual Cycle at All Sites in the NOAA Network

EMD decomposition allows us to separate the various frequency modes from the rest of the signal, as, for example, exemplified in Figure 3 for the case of the MLO station. The supplemental material for brevity shows the second mode or annual cycle and the rest of the EMD decomposition for the 14 NOAA stations.

Here we will summarize the analysis of the annual cycle based on the fit with a pure harmonic wave of period T,

$$A\sin((2\pi(t-d))/T) \tag{4}$$

with the time t in units of months and $T = 12$ months; the amplitude and delay A, d are fit parameters. To phase the harmonic with the calendar year, the fit considers the data from January 2001, $(t = 1)$ up to Decem-

Table 2
Amplitude and Delay of the Annual Cycle Fitted With a Pure Harmonic Wave With a Period T = 12 Months (See Equation 4)

					Annual cycle amplitude and delay		
Station	Code	Lat (°N)	Lon (°W)	Elevation (masl)	Amplitude, A (ppt)	Delay, d (months)	Corr. Coef. R^2
Alert, Nunavut, Canada	ALT	82.4508	62.5072	185	43.54 [42.36, 44.71]	1.00 [0.95, 1.05]	0.96
Point Barrow, USA	BRW	71.3230	156.6114	11	45.04 [43.92, 46.15]	0.93 [0.88,0.96]	0.96
Cape Grim, Tasmania	CGO	−40.683	144.6900	94	16.32 [15.93, 16.71]	−0.76 [−0.81, −0.72]	0.97
Harvard Forest, USA	HFM	42.5378	72.1714	340	54.79 [53.72, 56.26]	−0.27 [−0.33, −0.22]	0.96
Cape Kumukahi, USA	KUM	19.7371	155.0116	0.30	20.77 [19.79, 21.74]	1.78 [1.69, 1.87]	0.88
Park Falls, USA	LEF	45.9451	90.2732	472	46.44 [44.73, 48.15]	0.13 [0.06, 0.20]	0.92
Mace Head, Ireland	MHD	53.3260	9.899	5.00	32.58 [30.97, 34.20]	0.94 [0.85, 1.04]	0.88
Mauna Loa, USA	MLO	19.5362	155.5763	3,397	17.27 [16.51, 18.03]	1.92 [1.85, 2.00]	0.90
Niwot Ridge, USA	NWR	40.0531	105.5864	3,523	20.24 [19.4, 21.08]	1.45 [1.37, 1.53]	0.90
Palmer Station, Antarctica	PSA	−64.7742	64.0527	10	18.82 [18.11, 1952]	−0.87 [−0.94, −0.80]	0.92
Tutuila, American Samoa	SMO	−14.2474	170.5644	42	8.53 [7.82, 9.23]	−0.33 [−0.50, −0.18]	0.71
South Pole, Antarctica	SPO	−89.98	24.8	2810	[12.59] [11.94,13.24]	−0.34 [−0.44, −0.24]	0.86
Summit, Greenland	SUM	72.5962	38.422	3,209	31.18 [30.21,32.15]	0.83 [0.77, 0.96]	0.96
Trinidad Head, USA	THD	41.0541	124.151	107	43.37 [41.37, 45.36]	1.91 [1.82, 2.00]	0.90

Note. The pure harmonic has a max and min in March and September, respectively. The values in square brackets give the 95% confidence interval, whereas R^2 is the correlation coefficient.

ber 2020 ($t = 240$). A Least Squares fitting procedure of the model of Equation 4 to the IMF2 data (e.g., see Figure 3) yields for the MLO station $A = 17.27$ ppt, with a 95% confidence interval of [16.51, 18.03] ppt and, $d = 1.93$ months, with a 95% confidence interval of [1.85, 2.00] months. The goodness of the fit has been assessed through the correlation coefficient, and we found $R^2 = 0.90$. Because of its definition, the pure harmonic of Equation 4 has its peak (maximum) in March and its trough (minimum) in September. Therefore, the delay $d \sim 2$ months says that the peak value is attained in May, whereas the trough is in November. Furthermore, on average, the annual cycle's peak-to-peak amplitude is equal to ∼34 ppt in the MLO measurement record.

The analysis for the other stations is summarized in Table 2. The goodness of the fit also allows us to check for possible inter-annual variability that changes the annual cycle's year-to-year amplitude. In this respect, we see from Table 2 that the correlation coefficient of the fit with Equation 4 is, for most sites, larger than 0.90, apart from SMO, for which the value is 0.71. SMO is notably different likely because of its proximity to the equator and the large interannual variability in the position of convergence zones, particularly in December–March, that affects mole fraction measurements at SMO for many gases having significant hemispheric mole fraction differences. We also quote that in the period Dec-Mar, we have the peak of OCS formation from DMS oxidation (Jernigan et al., 2022), which could explain why SMO (a tropical oceanic station) is so peculiar.

For the other 13 stations, a pure harmonic wave accounts for most of the dynamic of the annual cycle. As expected, the cycle's amplitude has a robust latitudinal gradient because continents and anthropogenic sources are concentrated in the Northern Hemisphere. However, there is also a significant difference in the cycle phase. In the southern hemisphere, the phase d is negative, and the peak of OCS is around February. This behavior agrees with the dominance of the ocean for setting the phasing of OCS mole fraction in the southern hemisphere (Montzka et al., 2007) and current OCS ocean emission inventory by Lennartz et al. (2021), which shows that the globally integrated monthly fluxes for the austral hemisphere are highest in summer and lowest in winter. In the Northern Hemisphere, in most cases, the delay is positive and close to $d = 1$ month, which positions the OCS peak in April. For the two Eastern American stations, LEF and HFM, $d \approx 0$, which is likely the effect of their position in the area of natural forest sinks. Overall, the latitudinal dependencies for amplitude and phase agree with the findings of other studies (e.g., Hannigan et al., 2022).

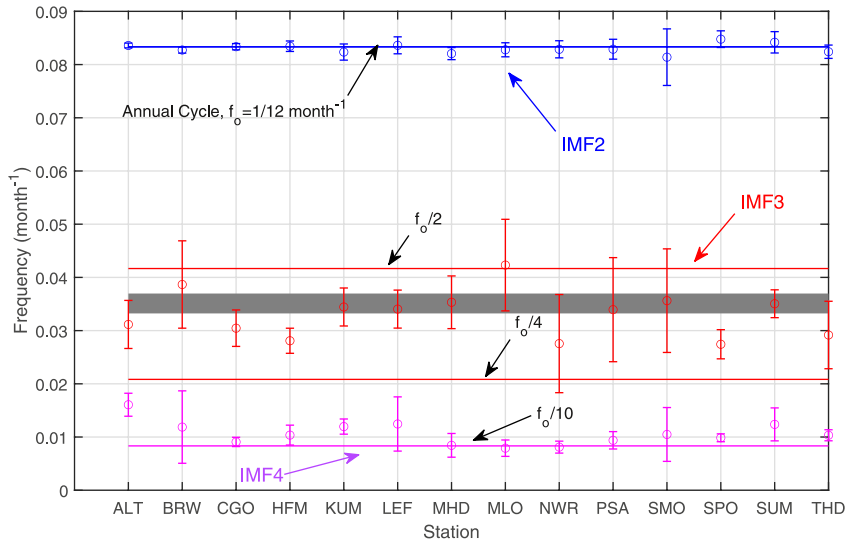

Figure 7. Peak frequencies of the IMF from 2 to 4 as a function of the station. The figure also shows the subtone frequencies of the annual cycle f_o, that is $f_o/2$, $f_o/4$, and $f_o/10$ to identify where the observed peak frequencies accumulate. The gray area gives the range of the QBO mean cycle, which has a periodicity of 28–29 months.

3.3. Oscillatory Modes at All Sites in the NOAA Network and the Role of the Third EMD Mode

The previous sections have mainly focused on assessing the annual cycle's prominent role due to the summer OCS drawdown by terrestrial vegetation. However, EMD analysis has also revealed other frequency modes lower than the annual cycle. In principle, this rich variability could be associated with climate characteristic scales such as the QBO (∼2 years), El-Nino (∼2 − 7 years), or simply interannual variability linked to biogenic activities. The in-depth analysis of these modes is not the present study's focus. However, we highlight them here to benefit the reader and to incite further studies. The peak frequencies of the IMF 2–4 are summarized in Figure 7 as a function of the station. From Figure 7, we see a great consistency among the various stations. As already said, the IMF2 represents the annual cycle, with frequency $f_o = \frac{1}{12} = 0.0833\,\text{month}^{-1}$, and we see that IMF2 at all stations peaked at this frequency. In Figure 7, we have also drawn the sub-tone frequency, $f_o/2$, $f_o/4$ and $f_o/10$ to help to identify where the observed peak frequencies accumulate.

It is seen that the IMF4 tends to accumulate at the frequency $f_o/10$, which is lower than the threshold frequency, f_{th}. In effect, the IMF4 has been moved to the trend τ, according to its definition of Equation 3.

Much more interesting is the behavior of the IMF3, which shows good consistency with the QBO mean cycle (28 months timescales, e.g., Baldwin et al., 2001). The quasi-biennial oscillation (QBO) is a quasi-periodic oscillation of the equatorial zonal wind between easterlies and westerlies in the tropical stratosphere. According to Ray et al. (2020), for trace gases with atmospheric lifetimes longer than a month (and OCS is a trace gas with a lifetime of 1.5–3 years), QBO can be the primary mode of variability in the stratosphere-to-troposphere exchange on 1- to 5-year timescales for certain gases having stratospheric losses, such as the chlorofluorocarbons and nitrous oxide. The QBO influence on tropospheric abundance arises from the modulation of the stratosphere to troposphere mass flux. The modulation can appear in surface measurements and drives the interannual variability of some trace gases that have strong mole fraction gradients across the tropopause. The effect has been demonstrated in chemistry-climate model simulations of chlorofluorocarbon-11, chlorofluorocarbon-12, and nitrous oxide (see also Ruiz et al., 2021). Our analysis could be the first experimental evidence that a mode of variability compatible with QBO is found in the OCS monthly means.

The standard approach that defines the QBO anomaly uses the equatorial zonal winds at a single pressure level (normally 50 hPa) and its analysis shows a period that varies from 22 to 34 months with an average of slightly more than 28 months. We stress that the third IMF also shows a varying period, which can be easily seen by comparing, for example, the third IMF to the second one in Figure 3. The same comparison can be performed for all stations using the EMD decomposition provided in the supplemental material. An analysis of Figure 3 shows

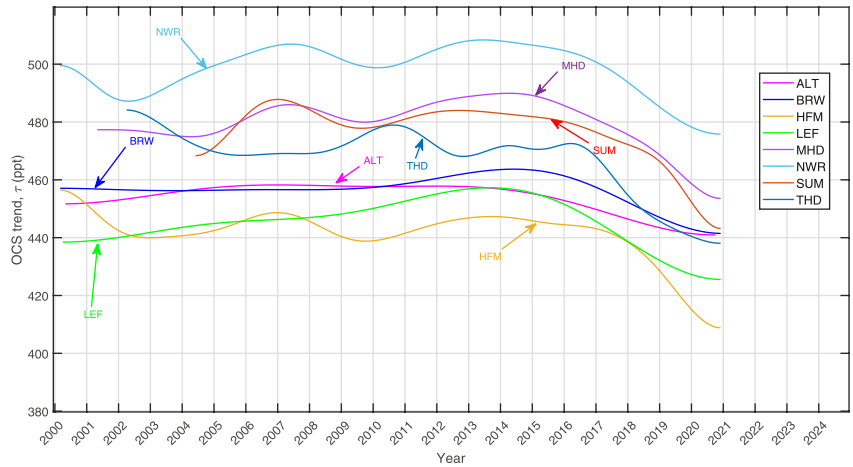

Figure 8. EMD-derived trend determination, τ component (Equation 3), for OCS measured at stations in the Northern Hemisphere at latitudes greater than 30°N.

that the distance between two consecutive peaks varies from 13 to 27 months, with an average of 22 months and a standard deviation of about 4.5 months.

A better agreement with the QBO average frequency is seen with the other two (sea level) tropical stations of KUM and SMO. Figure 7 shows that the QBO average frequency perfectly agrees with those of these two stations. The EMD decomposition allows us to filter out from the original OCS time series all components or modes with variability shorter than ∼22 months and larger than ∼34 months and yields the third IMF, which quantifies the OCS variability supposedly associated with QBO. For example, from Figure 3, which refers to the MLO station, we see that this component has a peak-to-peak amplitude of ∼20 ppt. Considering the data in Figure 3 again, we estimate for the third IMF a variance of 17.17 ppt^2, which can be compared to the total variance of the OCS times series of 320.41 ppt^2. An analysis of how the frequency changes with time can also be addressed using the Huang-Hilbert transform and an example is provided in the supplemental material (e.g., see Figures S32 and S33 in Supporting Information S1) The third IMF quantifies the QBO potential effect related to its influence on atmospheric mixing processes (Ray et al., 2020). However, we stress that IMF3 variability and frequency mode could also be connected to the interplay of biogenic natural sources and sinks, as evidenced in the recent works by Lennartz et al. (2021) and Vesala et al. (2022). Further work is needed to confirm this link to the QBO, for example, also considering OCS in the stratosphere and an in-depth correlation study with the QBO anomaly.

3.4. The Long-Term EMD Component, τ at All Sites in the NOAA Network

To have a more general and possibly global picture, Figure 8 shows the EMD trend, τ, for the North-Hemisphere stations north of 30°N of the NOAA network. All Northern stations consistently show a decreasing atmospheric OCS mole fraction from 2015 to 2020.

The long-term component is always relevant in terms of explained variance in these data at all sites, as shown in Table 2. In terms of standard deviation, the trend τ explains more than ∼15% of the variability of the whole signal, $X(j), j = 1, \ldots, N$. We stress that the long-term components' variability in Figure 8 reflects a good general agreement with original data. The overall mean is not distorted and long-term local features at the scale of the threshold frequency are well reproduced. This is exemplified in Figure 9 for the case of the NWR station. In Figure 9, we also show a comparison with the *lowess* trend, τ_l, which as for the case of the MLO station smooths the features at the scale of the threshold frequency, $f_{th} = 3/N$. For the sake of brevity, the comparison between τ and τ_l is not shown in the paper for all stations. Nevertheless, the supplemental material has provided this comparison for the interested reader. Here we stress that the *lowess* smoothing agrees with EMD in detecting a decline in OCS atmospheric column amount since 2015–2016. However, to mark the difference and advantage of EMD upon the *lowess* trend, we should consider that the correct cut-off for the lowess trend we show has been prescribed as a result of the frequency modes determined through our EMD analysis.

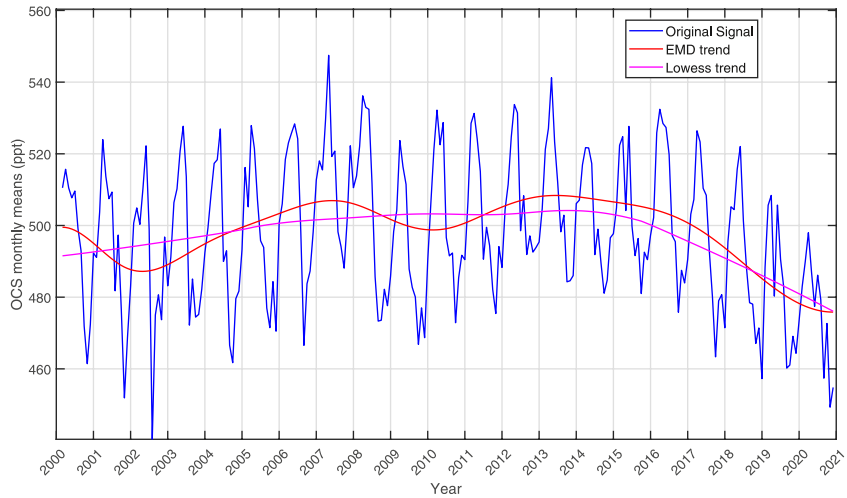

Figure 9. OCS monthly averages (2000–2020) for the NWR station and trend analysis according to EMD (Equation 3) and the non-parametric *lowess* approach (see text in the paper).

The results for the stations between 30°N and 30°S are shown in Figure 10. Consistent with what has been shown for the Northern Hemisphere north of 30°N, we see a decreasing trend for the three stations from 2015 to 2016 through 2020.

Finally, Figure 11 shows the results for the three stations in the Southern Hemisphere. Also in this case, we have that the three stations show a negative trend since 2015–2016, which is strongly consistent with the findings we have shown for the other NOAA stations after these years.

An essential aspect of the analysis we have shown with the 20-year long time series is the presence of a relatively large variance of the OCS signal at frequencies below the threshold $f_{th} = \frac{3}{N}$ which may reflect scales of the general atmospheric circulation, the climate forcing or even the long-term changes in the magnitude of overall or total OCS emissions (e.g., Zumkehr et al., 2018).

The low-frequency variability is shown in Table 3 in terms of the standard deviation, that is, the variability strength, of the EMD trend τ (computed according to Equation 3) and the original monthly observations, $X(j), j = 1, \ldots, N$.

From Table 3, we see that the trend or long-term variability is between ∼15%–40% of the total power of the signal. Therefore, this component is not negligible concerning the yearly cycle. In effect, from Figures 8–11, we

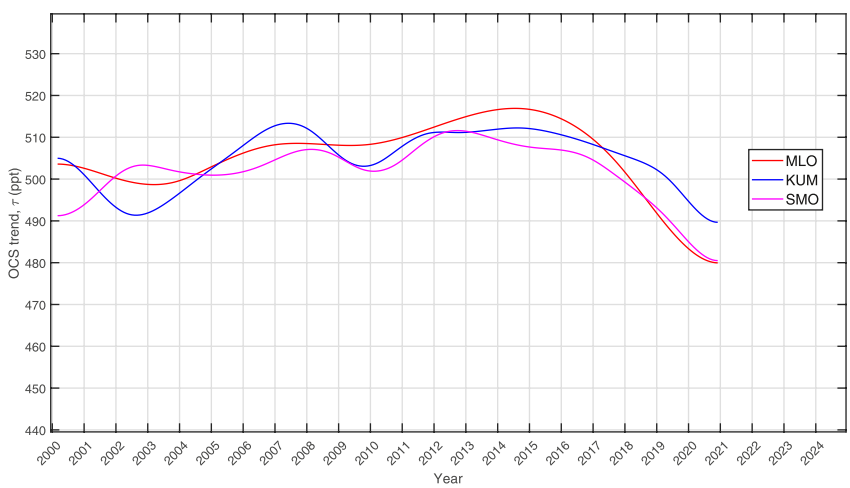

Figure 10. EMD-derived trend determination, τ component (Equation 3) for the NOAA stations between 30°N and 30°S.

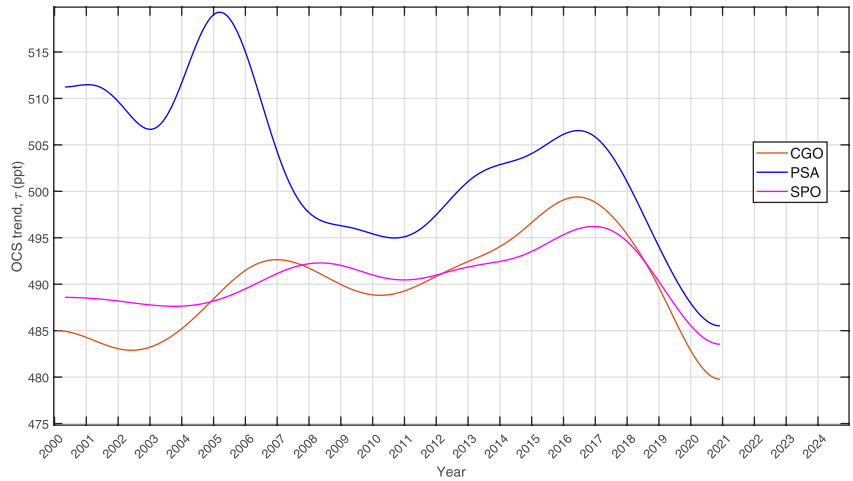

Figure 11. Trend analysis for OCS measured at sites in the Southern Hemisphere. We note that for PSA, the trend seems to have reversed from a decreasing one since about 2010. However, it is likely that the trend at PSA is influenced by contamination in sampling equipment used at that site in the first half of the record (2000–2010). The sample-to-sample variability in the PSA record is much noisier prior to 2010 than after it, consistent with that conclusion.

see that the variability has consistently increased in the last few years, which leads us to conclude that the OCS mole fraction has entered a worldwide decreasing phase. These findings suggest a recent broad-scale atmospheric decline captured by measurements at all NOAA sites.

To sum up, we can say that the 20-year OCS record at all sites shows a consistent low-frequency component, which yields a complex behavior with a generally increasing trend up to 2015, a temporary decrease during 2009, and finally, a decline in the last 6–7 years. As Hannigan et al. (2022) suggested, these common global trend features may reflect an imbalance in total OCS sources and losses. In this respect, Hannigan et al. (2022) have shown that the lower troposphere variability of OCS has a statistically significant correlation (correlation coefficient ranging from 0.46 to 0.77) with the revised anthropogenic emissions budget of Zumkehr et al. (2018)

Table 3
Variability (in Terms of Standard Deviation) of the EMD Trend τ (Equation 3) and the Original Signal, $X(j), j = 1, \ldots, N$, for the 20 Year-Long Time Series Analyzed in This Paper

					Variability (ppt)		
Station	Code	Lat (°N)	Lon (°W)	Elevation (masl)	Trend, τ	Signal, $X(j)$	% ratio trend/signal
Alert, Nunavut, Canada	ALT	82.4508	62.5072	185	5.38	39.64	13.6
Point Barrow, USA	BRW	71.3230	156.6114	11	6.34	40.87	15.5
Cape Grim, Tasmania	CGO	−40.683	144.6900	94	4.26	14.76	28.8
Harvard Forest, USA	HFM	42.5378	72.1714	340	8.34	49.53	16.8
Cape Kumukahi, USA	KUM	19.7371	155.0116	0.30	6.10	22.48	27.1
Park Falls, USA	LEF	45.9451	90.2732	472	9.62	44.77	21.4
Mace Head, Ireland	MHD	53.3260	9.899	5.00	7.00	33.35	20.9
Mauna Loa, USA	MLO	19.5362	155.5763	3,397	6.98	17.90	38.9
Niwot Ridge, USA	NWR	40.0531	105.5864	3,523	7.65	19.91	38.4
Palmer Station, Antarctica	PSA	−64.7742	64.0527	10	8.52	20.03	42.5
Tutuila, American Samoa	SMO	−14.2474	170.5644	42	5.80	12.85	45.1
South Pole, Antarctica	SPO	−89.98	24.8	2810	2.65	14.69	6.40
Summit, Greenland	SUM	72.5962	38.422	3,209	8.24	34.19	24.1
Trinidad Head, USA	THD	41.0541	124.151	107	9.95	41.40	24.0

between 1986 and 2012. Also, they conclude that a slowing of anthropogenic emissions is likely the cause of the actual worldwide phase of decline.

It is also interesting to note that the best estimates of natural sources and sinks of OCS in total would suggest slight increases in atmospheric mole fraction in recent years in the absence of the anthropogenic emission trends discussed above (e.g., Lennartz et al., 2021; Vesala et al., 2022). For example, based on simulation studies, Lennartz et al. (2021) show that decadal oceanic emissions of OCS are mainly driven (correlation coefficient 0.94) by chromophoric dissolved organic matter (CDOM) and skin temperature (correlation coefficient 0.41). Equivalent results are also obtained for CS_2, whose atmospheric oxidation (e.g., Chin & Davis, 1993), represents an additional source of OCS. Although the ocean emissions have seasonal and interannual variability, along with spatial patterns with a minimum in the tropics (because of the higher skin temperature), the global trend over the period 2000–2019 in OCS emission is believed to be slightly increasing (Lennartz et al., 2021). On the same line is the recent study by Hattori et al., 2020. By constraining the OCS budget with sulfur isotopes, they show that anthropogenic sources, not merely oceanic sources, can account for much of the missing source of atmospheric OCS.

Regarding sinks, Vesala et al. (2022) finds that long-term fluxes of OCS, their seasonality, and interannual variability in boreal forests are strongly correlated with meteorological conditions (correlation ranging between 0.77 and 0.88). Because of climate change, the summer season has largely drifted toward long-lasting droughts. Droughts have significantly reduced ecosystem-scale OCS uptake. In this respect, the Copernicus Climate Change Service (C3S) data set (e.g., see https://climate.copernicus.eu/esotc/2021/globe-in-2021 (accessed on 15 August 2022)) indicates that the last 7 years have been the warmest on record.

All of this evidence related to long-term global fluxes of OCS lead us to conclude that a slowing in anthropogenic sources can explain the worldwide decline phase, as Hannigan et al. (2022) first suggested.

4. Conclusions

This study analyzed the monthly average time series of OCS using data from the globally distributed NOAA/GML network stations between 2000 and 2020. The analysis has been performed by using the EMD, which decomposes a given time series in its primary cycles plus a trend. The method is non-parametric, and there is no need to specify a trend model as generally done with other approaches.

However, EMD still has some open issues regarding its formal characterization when operating on a broadband signal, such as white noise (e.g., Wu & Huang, 2010). In our analysis, this issue has been minimized by resorting to decomposition, which, while non-exact, still provides an approximation of the given signal (Wang et al., 2010). The EMD method we use to calculate the decomposition has been implemented with the two basic stopping criteria recommended by Wang et al. (2010) *to obtain physically meaningful results.* The stopping rules include a Cauchy criterion (e.g., Wang et al., 2010), to stop the iteration from getting a given IMF, and an Energy ratio criterion (e.g., Wang et al., 2010), to stop the EMD decomposition. In this way, as stressed by Wang et al. (2010), the EMD implementation yields an approximation concerning the cubic spline basis but avoids resulting in IMFs that have no physical significance.

In addition, we remark that other problems could affect EMD performance in practice (Huang et al., 1998, 2003), especially in measurement noise. One limitation is the difficulty of carrying out a clean separation in IMFs when their local frequencies are too close (e.g., Stallone et al., 2020). In some cases, this separation could be improved by applying the so-called EEMD (Wu & Huang, 2009), an approach in this paper that adds random noise to the observations.

We constrain EMD by specifying the maximum number of modes and a frequency threshold to separate lower frequencies from the annual cycle. In effect, the stopping criteria (Wang et al., 2010) embedded in the most updated EMD software tool by Matlab (we used release 2020b in this study) do not provide a reliable strategy to separate the trend from pure modes. Therefore, we have shown that frequency thresholding and a suitable limitation of modes are *best practices* for the successful use of EMD.

With this in mind, the decomposition in cyclic modes of the OCS series has shown the presence of low-frequency time scales of ∼10 years. Furthermore, the low-frequency component yields a long-range time evolution, indicating a decline in OCS concentration in the atmosphere in the last 6–7 years. The reduction is seen in data

obtained from all stations examined in the present work, consistent with a current imbalance in total global OCS sources and losses (e.g., Hannigan et al., 2022). Moreover, we have shown that the OCS records exhibit a cyclic mode between 2 and 4 years, which may be linked to the Quasi Biennal Oscillation (QBO). However, this variability could also be connected to the interplay of biogenic natural sources and sinks, as stated in the recent analysis by Lennartz et al. (2021) and Vesala et al. (2022). An important aspect of the mode between 2 and 4 years is the frequency changing with time. This characteristic has been assessed by analyzing consecutive peaks of the related IMF (the third one) and using the Huang-Hilbert transform. We stress that the quasi-periodic processes are peculiar to the dynamics of the atmosphere and its coupling with land and ocean. Unlike EMD, these kinds of processes cannot be analyzed with the usual Fourier analysis, which once again stresses the advantage of EMD.

In addition, a decreasing trend of OCS mole fraction has been observed in the last 6–7 years at all NOAA/GML measurement sites, which could also be related to the integrated effect of slowing anthropogenic emissions, as suggested by Hannigan et al. (2022). As indicated by Lennartz et al. (2021) and Vesala et al. (2022), the interplay of sources and sinks is also influenced by climate change. As a result, the atmospheric OCS concentration will likely keep changing globally. Because the OCS mole fraction is involved in forming stratospheric sulfate aerosol, continuous observation of the OCS mole fraction is useful for characterizing changes in this stratospheric layer.

Moreover, an analysis using EMD led to the discovery of new OCS variations. EMD may apply to other atmospheric gases, such as CO_2 as well. An essential aspect of EMD is the possibility to insulate, for example, the seasonal cycle from other variability modes, which could allow us to compare and correlate the process from different gases, for example, OCS and CO_2.

Finally, no matter the origin of the present OCS mole fraction decline, the carbonyl sulfide atmospheric budget is currently unbalanced. Recent works by Hattori et al. (2020), Lennartz et al. (2021), and Vesala et al. (2022) have suggested refining sources and sinks magnitude, which could lead to a better understanding of the atmospheric OCS budget. However, these new sources and sinks would increase the OCS trend, which is not the case based on actual observations. We think that further analysis of global transport coupled with emission-chemistry models could yield new insights in light of the most recent changes we have identified and assessed in this study. We have shown that the typical representation of OCS dynamics with a long-term trend plus a seasonal cycle is less helpful in identifying other modes of variability. These modes are likely related to atmospheric dynamics and variations in anthropogenic and natural OCS sources and sinks (e.g., Hannigan et al., 2022; Lennartz et al., 2021; Ray et al., 2020; Vesala et al., 2022).

Data Availability Statement

The OCS data used in the paper are freely available from the GML Global Monitoring Laboratory program that measure OCS at the website http://www.esrl.noaa.gov/gmd/hats/gases/OCS.html. (Global Monitoring Laboratory, 2022) *Data* - http://www.esrl.noaa.gov/gmd/hats/gases/OCS.html.

Acknowledgments
Measurements from flasks from the 14 stations listed in Table 1 have been downloaded from the website http://www.esrl.noaa.gov/gmd/hats/gases/OCS.html. We give credit to the National Oceanic and Atmospheric Administration (NOAA)/ Global Monitoring Laboratory (GML) in Boulder as a source of the data and appreciate the technical assistance of B. Hall, C. Siso, and I. Vimont, for assisting with creating and maintaining a reliable long-term atmospheric history of OCS mole fraction. This research was carried out in the framework of the project "OT4CLIMA" which was funded by the Italian Ministry of Education, University and Research (D.D. 2261 del 6.9.2018, PON R&I 2014-2020 and FSC). Open Access Funding provided by Universita degli Studi della Basilicata within the CRUI-CARE Agreement.

References

Aydin, M., Britten, G. L., Montzka, S. A., Buizert, C., Primeau, F., Petrenko, V., et al. (2020). Anthropogenic impacts on atmospheric carbonyl sulfide since the 19th century inferred from polar firn air and ice core measurements. *Journal of Geophysical Research: Atmospheres*, *125*(16), e2020JD033074. https://doi.org/10.1029/2020JD033074

Baldwin, M., Gray, L., Dunkerton, T., Hamilton, K., Haynes, P., Randel, W., et al. (2001). The quasi-biennial oscillation. *Reviews of Geophysics*, *39*(2), 179–229. https://doi.org/10.1029/1999RG000073

Berry, J., Wolf, A., Campbell, J. E., Baker, I., Blake, N., Blake, D., et al. (2013). A coupled model of the global cycles of carbonyl sulfide and CO_2: A possible new window on the carbon cycle. *Journal of Geophysical Research: Biogeosciences*, *118*(2), 842–852. https://doi.org/10.1002/jgrg.20068

Brühl, C., Lelieveld, J., Crutzen, P. J., & Tost, H. (2012). The role of carbonyl sulphide as a source of stratospheric sulphate aerosol and its impact on climate. *Atmospheric Chemistry and Physics*, *12*(3), 1239–1253. https://doi.org/10.5194/acp-12-1239-2012

Campbell, J. E., Berry, J. A., Seibt, U., Smith, S. J., Montzka, S. A., Launois, T., et al. (2017). Large historical growth in global terrestrial gross primary production. *Nature*, *544*(7648), 84–87. https://doi.org/10.1038/nature22030

Campbell, J. E., Carmichael, G. R., Chai, T., Mena-Carrasco, M., Tang, Y., Blake, D. R., et al. (2008). Photosynthetic control of atmospheric carbonyl sulfide during the growing season. *Science*, *322*(5904), 1085–1088. https://doi.org/10.1126/science.1164015

Campbell, J. E., Whelan, M. E., Seibt, U., Smith, S. J., Berry, J. A., & Hilton, T. W. (2015). Atmospheric carbonyl sulfide sources from anthropogenic activity: Implications for carbon cycle constraints. *Geophysical Research Letters*, *42*(8), 3004–3010. https://doi.org/10.1002/2015GL063445

Camy-Peyret, C., Liuzzi, G., Masiello, G., Serio, C., Venafra, S., & Montzka, S. A. (2017). Assessment of IASI capability for retrieving carbonyl sulphide (OCS). *Journal of Quantitative Spectroscopy and Radiative Transfer*, *201*, 197–208. https://doi.org/10.1016/j.jqsrt.2017.07.006

Capparelli, V., Franzke, C., Vecchio, A., Freeman, M. P., Watkins, N. W., & Carbone, V. (2013). A spatiotemporal analysis of U.S. station temperature trends over the last century: On the temperature trends over the United States. *Journal of Geophysical Research: Atmospheres*, *118*(14), 7427–7434. https://doi.org/10.1002/jgrd.50551

Chin, M., & Davis, D. D. (1993). Global sources and sinks of OCS and CS2 and their distributions. *Global Biogeochemical Cycles*, *7*(2), 321–337. https://doi.org/10.1029/93GB00568

Cleveland, W. S., & Devlin, S. J. (1988). Locally-weighted regression: An approach to regression analysis by local fitting. *Journal of the American Statistical Association*, *83*(403), 596–610. https://doi.org/10.2307/2289282

Gardiner, T., Forbes, A., de Mazière, M., Vigouroux, C., Mahieu, E., Demoulin, P., et al. (2008). Trend analysis of greenhouse gases over Europe measured by a network of ground-based remote FTIR instruments. *Atmospheric Chemistry and Physics*, *8*(22), 6719–6727. https://doi.org/10.5194/acp-8-6719-2008

Global Monitoring Laboratory. (2022). Halocarbons and other atmospheric trace species [Dataset]. Global Monitoring Laboratory. Retrieved from https://gml.noaa.go/hats/gases/OCS.html

Hannigan, J. W., Ortega, I., Shams, S. B., Blumenstock, T., Campbell, J. E., Conway, S., et al. (2022). Global atmospheric OCS trend analysis from 22 NDACC stations. *Journal of Geophysical Research: Atmospheres*, *127*(4), e2021JD035764. https://doi.org/10.1029/2021JD035764

Hattori, S., Kamezaki, K., & Yoshida, N. (2020). Constraining the atmospheric OCS budget from sulfur isotopes. *Proceedings of the National Academy of Sciences*, *117*(34), 20447–20452. https://doi.org/10.1073/pnas.2007260117

Huang, N. E., Shen, Z., Long, S. R., Wu, M. C., Shih, H. H., Zheng, Q., et al. (1998). The empirical mode decomposition and the Hilbert spectrum for nonlinear and nonstationary time series analysis. *Proceedings of the Royal Society of London. Series A: Mathematical, Physical and Engineering Sciences*, *454*(1971), 903–995. https://doi.org/10.1098/rspa.1998.0193

Huang, N. E., Wu, M.-L. C., Long, S. R., Shen, S. S. P., Qu, W., Gloersen, P., & Fan, K. L. (2003). A confidence limit for the empirical mode decomposition and Hilbert spectral analysis. *Proceedings of the Royal Society of London. Series A: Mathematical, Physical and Engineering Sciences*, *459*(2037), 2317–2345. https://doi.org/10.1098/rspa.2003.1123

Jernigan, C. M., Fite, C. H., Vereecken, L., Berkelhammer, M. B., Rollins, A. W., Rickly, P. S., et al. (2022). Efficient production of carbonyl sulfide in the low-NO_x oxidation of dimethyl sulfide. *Geophysical Research Letters*, *49*(3), e2021GL096838. https://doi.org/10.1029/2021gl096838

Kettle, A. J. (2002). Global budget of atmospheric carbonyl sulfide: Temporal and spatial variations of the dominant sources and sinks. *Journal of Geophysical Research*, *107*(D22), 4658. https://doi.org/10.1029/2002JD002187

Kremser, S., Jones, N. B., Palm, M., Lejeune, B., Wang, Y., Smale, D., & Deutscher, N. M. (2015). Positive trends in Southern Hemisphere carbonyl sulfide. *Geophysical Research Letters*, *42*(21), 9473–9480. https://doi.org/10.1002/2015GL065879

Krysztofiak, G., Té, Y. V., Catoire, V., Berthet, G., Toon, G. C., Jégou, F., et al. (2015). Carbonyl sulphide (OCS) variability with latitude in the atmosphere. *Atmosphere-Ocean*, *53*(1), 89–101. https://doi.org/10.1080/07055900.2013.876609

Lejeune, B., Mahieu, E., Vollmer, M. K., Reimann, S., Bernath, P. F., Boone, C. D., et al. (2017). Optimized approach to retrieve information on atmospheric carbonyl sulfide (OCS) above the Jungfraujoch station and change in its abundance since 1995. *Journal of Quantitative Spectroscopy and Radiative Transfer*, *186*, 81–95. https://doi.org/10.1016/j.jqsrt.2016.06.001

Lennartz, S. T., Gauss, M., von Hobe, M., & Marandino, C. A. (2021). Monthly resolved modelled oceanic emissions of carbonyl sulphide and carbon disulphide for the period 2000–2019. *Earth System Science Data*, *13*(5), 2095–2110. https://doi.org/10.5194/essd-13-2095-2021

Maseyk, K., Berry, J. A., Billesbach, D., Campbell, J. E., Torn, M. S., Zahniser, M., & Seibt, U. (2014). Sources and sinks of carbonyl sulfide in an agricultural field in the Southern Great Plains. *Proceedings of the National Academy of Sciences*, *111*(25), 9064–9069. https://doi.org/10.1073/pnas.1319132111

Montzka, S. A., Aydin, M., Battle, M., Butler, J. H., Saltzman, E. S., Hall, B. D., et al. (2004). A 350-year atmospheric history for carbonyl sulfide inferred from Antarctic firn air and air trapped in ice. *Journal of Geophysical Research*, *109*(D22), D22302. https://doi.org/10.1029/2004JD004686

Montzka, S. A., Calvert, P., Hall, B. D., Elkins, J. W., Conway, T. J., Tans, P. P., & Sweeney, C. (2007). On the global distribution, seasonality, and budget of atmospheric carbonyl sulfide (COS) and some similarities to CO_2. *Journal of Geophysical Research*, *112*(D9), D09302. https://doi.org/10.1029/2006JD007665

Notni, J., Schenk, S., Protoschill-Krebs, G., Kesselmeier, J., & Anders, E. (2007). The missing link in COS metabolism: A model study on the reactivation of carbonic anhydrase from its hydrosulfide analogue. *ChemBioChem*, *8*(5), 530–536. https://doi.org/10.1002/cbic.200600436

Ogée, J., Sauze, J., Kesselmeier, J., Genty, B., Van Diest, H., Launois, T., & Wingate, L. (2016). A new mechanistic framework to predict OCS fluxes from soils. *Biogeosciences*, *13*(8), 2221–2240. https://doi.org/10.5194/bg-13-2221-2016

Protoschill-Krebs, G., & Kesselmeier, J. (1992). Enzymatic pathways for the consumption of carbonyl sulphide (COS) by higher plants. *Botanica Acta*, *105*(3), 206–212. https://doi.org/10.1111/j.1438-8677.1992.tb00288.x

Ray, E. A., Portmann, R. W., Yu, P., Daniel, J., Montzka, S. A., Dutton, G. S., et al. (2020). The influence of the stratospheric Quasi-Biennial Oscillation on trace gas levels at the Earth's surface. *Nature Geoscience*, *13*(1), 22–27. https://doi.org/10.1038/s41561-019-0507-3

Ruiz, D. J., Prather, M. J., Strahan, S. E., Thompson, R. L., Froidevaux, L., & Steenrod, S. D. (2021). How atmospheric chemistry and transport drive surface variability of N_2O and CFC-11. *Journal of Geophysical Research: Atmospheres*, *126*(8), e2020JD033979. https://doi.org/10.1029/2020JD033979

Schenk, S., Kesselmeier, J., & Anders, E. (2004). How does the exchange of one oxygen atom with sulfur affect the catalytic cycle of carbonic anhydrase? *Chemistry - A European Journal*, *10*(12), 3091–3105. https://doi.org/10.1002/chem.200305754

Stallone, A., Cicone, A., & Materassi, M. (2020). New insights and best practices for the successful use of Empirical Mode Decomposition, Iterative Filtering and derived algorithms. *Scientific Reports*, *10*(1), 15161. https://doi.org/10.1038/s41598-020-72193-2

Sun, Y. Y., Liu, H., Miyoshi, Y., Liu, L., & Chang, L. C. (2018). El Niño–Southern Oscillation effect on quasi-biennial oscillations of temperature diurnal tides in the mesosphere and lower thermosphere. *Earth Planets and Space*, *70*(1), 85. https://doi.org/10.1186/s40623-018-0832-6

Thoning, K. W., Tans, P. P., & Komhyr, W. D. (1989). Atmospheric carbon dioxide at Mauna Loa Observatory: 2. Analysis of the NOAA GMCC data, 1974–1985. *Journal of Geophysical Research*, *94*(D6), 8549–8565. https://doi.org/10.1029/JD094iD06p08549

Vesala, T., Kohonen, K.-M., Kooijmans, L. M. J., Praplan, A. P., Foltýnová, L., Kolari, P., et al. (2022). Long-term fluxes of carbonyl sulfide and their seasonality and interannual variability in a boreal forest. *Atmospheric Chemistry and Physics*, *22*(4), 2569–2584. https://doi.org/10.5194/acp-22-2569-2022

Wang, G., Chen, X.-Y., Qiao, F.-L., Wu, Z., & Huang, N. E. (2010). On intrinsic mode function. *Advances in Adaptive Data Analysis*, *2*(3), 277–293. https://doi.org/10.1142/S1793536910000549

Whelan, M. E., Lennartz, S. T., Gimeno, T. E., Wehr, R., Wohlfahrt, G., Wang, Y., et al. (2018). Reviews and syntheses: Carbonyl sulfide as a multi-scale tracer for carbon and water cycles. *Biogeosciences*, *15*(12), 3625–3657. https://doi.org/10.5194/bg-15-3625-2018

Wu, Z., & Huang, N. E. (2009). Ensemble empirical mode decomposition: A noise-assisted data analysis method. *Advances in Adaptive Data Analysis*, *1*(1), 1–41. https://doi.org/10.1142/S1793536909000047

Wu, Z., & Huang, N. E. (2010). On the filtering properties of the empirical mode decomposition. *Advances in Adaptive Data Analysis*, *2*(4), 397–414. https://doi.org/10.1142/S1793536910000604

Zumkehr, A., Hilton, T. W., Whelan, M., Smith, S., Kuai, L., Worden, J., & Campbell, J. E. (2018). Global gridded anthropogenic emissions inventory of carbonyl sulfide. *Atmospheric Environment*, *183*, 11–19. https://doi.org/10.1016/j.atmosenv.2018.03.063